PCCP

PAPER

View Article Online
View Journal | View Issue

Cite this: *Phys. Chem. Chem. Phys.*, 2024, **26**, 24912

Impact of coating type on structure and magnetic properties of biocompatible iron oxide nanoparticles: insights into cluster organization and oxidation stability†

Amal Nasser, *[ab] Asma Qdemat, [c] Harald Unterweger, [d] Rainer Tietze, [d] Xiao Sun, [e] Joachim Landers, [f] Juri Kopp, [f] Baohu Wu, [b] Marie-Sousai Appavou, [b] Anastasiia Murmiliuk, [b] Elliot Paul Gilbert, [g] Oleg Petracic *[c] and Artem Feoktystov *[b]

Received 26th April 2024,
Accepted 8th September 2024

DOI: 10.1039/d4cp01735h

rsc.li/pccp

Superparamagnetic iron oxide nanoparticles (SPIONs) are a promising tool for biomedical applications, including drug delivery, imaging, and magnetic hyperthermia. However, their tendency to agglomerate limits their performance efficiency. To overcome this limitation, a coating can be applied during or after synthesis. This work investigates the effect of three biocompatible coatings, namely sodium citrate, (3-aminopropyl)triethoxysilane (APTES), and dextran, on controlling the agglomeration of iron oxide nanoparticles. Various experimental techniques were used to characterize the structural and magnetic properties of the coated nanoparticles, including cryogenic transmission electron microscopy (cryo-TEM), magnetometry, Mössbauer spectroscopy, and small-angle X-ray and neutron scattering. The results indicate that the coatings effectively stabilize the nanoparticles, leading to clusters of different sizes that modify their magnetic behaviour due to magnetic inter-particle interactions. The oxidation kinetics of the nanoparticles prepared with the various coating materials were investigated to characterize their oxidation behaviour and stability over time. This research provides valuable insights into the design of an optimized nanoparticle functionalization strategy for biomedical applications.

1. Introduction

Magnetic nanoparticles can be manipulated by external magnetic fields and concentrated close to the targeted tissue, making them attractive for use *in vivo*. Superparamagnetic iron oxide nanoparticles (SPIONs) are a type of magnetic nanoparticles that show promise in theranostics, which combines therapy and diagnostics,[1–4] and find applications in various medical fields such as imaging, targeted drug delivery, and hyperthermia.[5–7] However, the development of these processes depends on a detailed understanding of the magnetic properties of the particles. These properties are influenced by various parameters, including particle size,[8] morphology,[9] crystalline defects (such as antiphase boundaries),[10] composition of iron oxide phases,[11] and interparticle interactions.[12]

Successful and reliable medical applications require the long-term stability of SPIONs. To achieve this goal, the particles are typically stabilized using electrostatic or steric coatings, which provide sufficient repulsion to avoid uncontrolled agglomeration.[13,14] textcolororange In addition it is important

[a] *Department of Physics, Technical University Munich (TUM), Garching, Germany*
[b] *Forschungszentrum Jülich GmbH, Jülich Centre for Neutron Science JCNS at MLZ, Garching, Germany. E-mail: a.nasser@fz-juelich.de, a.feoktystov@fz-juelich.de*
[c] *Forschungszentrum Jülich GmbH, Jülich Centre for Neutron Science JCNS-2, Jülich, Germany. E-mail: o.petracic@fz-juelich.de*
[d] *ENT Department, Section of Experimental Oncology and Nanomedicine (SEON), Else Kroener-Fresenius-Stiftung-Professorship, University Hospital Erlangen, Germany*
[e] *Deutsches Elektronen-Synchrotron DESY, 22607 Hamburg, Germany*
[f] *Faculty of Physics and Center for Nanointegration Duisburg-Essen (CENIDE), University of Duisburg-Essen, D-47057 Duisburg, Germany*
[g] *Australian Centre for Neutron Scattering, Australian Nuclear Science and Technology Organisation, NSW 2234, Australia*

† Electronic supplementary information (ESI) available: Histogram and lognormal fit for the distribution of individual particles as determined by TEM, FTIR spectra, the Mössbauer spectra for the B47 and D40 samples after different aging times of exposure to air, table of hydrodynamic size, polydispersity index (PDI) and zeta potential (mV), FTIR spectra, as well as ZFC/FC curves and SAXS curves for the fresh sample and after 6 months following preparation for the C71 sample. See DOI: https://doi.org/10.1039/d4cp01735h

to control the oxidation state.[15] Recently, controlled SPIONs agglomeration has gained substantial attention in research due to the improved magnetic response as a consequence of their larger size. Despite their larger size, these particles have a large degree of long-term stability.[16–18] Such systems are often termed 'clustered nanoparticles' or 'nanoflowers' and consist of smaller SPION constituents. Due to the single magnetic cores being closer together or even in contact, magnetic dipolar interactions are increased, or exchange interactions may be found.[19]

The most commonly used iron oxide phases for magnetic core nanoparticles in biomedical applications are magnetite Fe_3O_4 and maghemite γ-Fe_2O_3.[20] Both phases have a similar crystallographic structure (cubic inverse spinel) but exhibit different magnetic and electronic properties.[21,22] The presence of vacancies in maghemite and the variations in electronic configurations are responsible for the differences in magnetic properties. For instance, maghemite has a lower saturation magnetization of 76 A m^2 kg^{-1} compared to magnetite, which demonstrates a saturation magnetization of 87 A m^2 kg^{-1} at room temperature.[23]

Controlling specifically the oxidation state of the iron oxide cores is crucial for medical applications, as it significantly impacts their functionality. For example, the oxidation of magnetite to maghemite results in a reduction of the SPION's saturation magnetization. Also the magnetocrystalline anisotropy is affected. Consequently, both the efficiency of the particles and the reproducibility of results are altered.[24] Deliberate control of the oxidation state can hence lead *e.g.* to an increase of the heat delivery in magnetic hyperthermia applications.[25]

In our study, we have selected several coating agents, such as negatively charged citrate, positively charged APTES, and neutral hydrophilic polymer dextran, to stabilize the magnetic nanoparticles and control the magnetite oxidation. While numerous studies have explored the impacts of these coatings on cluster formation and the resulting physicochemical properties of magnetic nanoparticles,[26–32] the specifics of their magnetic properties remain debated.[33,34] To investigate the influence of particle size, structural organization, and aging on the magnetic properties of these clusters in detail, we employed magnetometry combined with small-angle X-ray scattering (SAXS) and cryogenic transmission electron microscopy (cryo-TEM). Additionally, we utilized small-angle neutron scattering (SANS) to examine the magnetic structure of the clustered particles for the citrate-coated system. In addition, we employ Mössbauer spectroscopy combined with magnetometry to investigate the time-dependent oxidation behavior of the particle-coating species. This approach hence provides information on the aging process, from storage to the final product. By using both Mössbauer spectroscopy and magnetometry, we were able to track the changes in Fe^{2+} and Fe^{3+} composition as a function of time for various coating types, determining the net magnetic properties and examining how fast this oxidation takes place and the proportion of the oxidized form.

2. Materials and methods

2.1. Synthesis of iron oxide nanoparticles

The iron oxide particles used in this study were prepared *via* the co-precipitation method.[35] This synthesis route was chosen for its simplicity, higher yield, and relatively low cost.[36–38] Initially, a mixture of $FeCl_2$ and $FeCl_3$ with a 1 : 2 molar ratio was dissolved in distilled water and stirred in an argon atmosphere to prevent oxidation. Subsequently, an ammonia solution (25%) was added for the precipitation reaction of the iron oxide. In the following stage, the corresponding coating materials were added to the solution to optimize the surface coating and control the cluster size, including citrate molecules, (3-aminopropyl)triethoxysilan (APTES), and dextran. The coated particles were dispersed in water and then sealed in containers under N_2 gas for the aging study, while others were filled under atmospheric conditions. Below is a summary of the materials' details.

2.1.1. Citrate-coating (C71). After the formation of the precipitate of iron oxide particles, 1 M sodium citrate solution was added, and the resulting solution was stirred at 90 °C for 30 minutes. The source of the materials used in preparation is found in ref. 14. The excess sodium citrate was removed by washing the resulting particles with acetone, followed by a drying process at room temperature to obtain the nanoparticle powder. The powder particles were subsequently dissolved in water with a concentration of 23 mg ml^{-1} of iron content and filtered using a syringe filter with a 0.2 μm – pore diameter.

2.1.2. (3-Aminopropyl)triethoxysilan (APTES)-coating (B47). 1 M APTES solution was added after stirring a suspension of iron oxide particles precipitate at 70 °C for 15 minutes. The suspension was then stirred for another 3 hours before cooling to room temperature. The source of the materials used is found in ref. 29. The prepared particles were washed three times with water and filtered through a syringe filter with a 0.8 μm – pore diameter. The concentrated particles were then dispersed in water with a concentration of 21 mg ml^{-1} of iron content, the pH value adjusted to 7.4, and the suspension stored at 4 °C.

2.1.3. Dextran-coating (D40). 0.006 M dextran solution was added to the reaction mixture before the precipitation of iron oxide nanoparticles. The mixture was then cooled to 4 °C, and the ammonia solution was added, resulting in a greenish suspension of iron hydroxide. The greenish suspension was heated to 75 °C for 40 minutes, leading to the transformation to iron oxide and a color change to dark brown. To remove excess ammonia and ion residues, the suspension was transferred to a dialysis bag and dialyzed against 4 L of water for 24 h, changing the water 5 times. Subsequently, the excess dextran from the supernatant was removed by ultrafiltration in a 5430R Eppendorf centrifuge. To increase steric stability, the dextran coating of the particles was cross-linked with epichlorohydrin and 5 M NaOH was added. The concentrated particle solution was filtered using a syringe filter with 0.22 μm – pore diameter. The nanoparticles were then dispersed in water to a concentration of 8.8 mg ml^{-1} of iron content and stored at 4 °C until further use. The source of materials used here is found in ref. 28.

2.2. Characterization methods

2.2.1. Cryogenic-transmission electron microscopy. A 4 μl droplet of SPIONs in a water solution with a concentration of 5.5 mg ml^{-1} was deposited onto a perforated carbon-coated grid in a thermal chamber with controlled relative humidity at atmospheric pressure. The grid was then blotted with filter paper and quickly plunged into liquified ethane. This ensures that particles are trapped in a thin layer of amorphous (non-crystalline) ice of *ca.* 100 nanometers. The grid was then transferred to a cryo-holder and placed in a transmission electron microscope (TEM) under vacuum. The images were taken using a cryo-TEM system (JEM-FS2200) with a G910 multi-position specimen cryo-holder using an acceleration voltage of 200 keV. The particle size and size distribution of approximately 200 core nanoparticles were measured using ImageJ software.

2.2.2. Magnetization measurements. Field and temperature dependent macroscopic magnetization measurements were conducted using a superconducting quantum interference device (SQUID) magnetometer (MPMS XL, Quantum Design) with 20 μl of 5.5 mg ml^{-1} iron dispersion in water. The dispersion was sealed in a polypropylene capsule fixed in a plastic straw sample holder. The magnetization was measured as a function of the magnetic field at 300 K, and 5 K, in a field range from −1.5 T to +1.5 T. To characterize the particle size distribution and interparticle interaction, magnetization measurements were recorded in zero-field-cooled (ZFC) and field-cooled (FC) regimes in a temperature range of 5 K to 225 K. This temperature range is well below the melting point of water and thus the particle clusters remain in an immobilized state. In order to avoid the formation of large domains of ice crystals, which would lead to an unwanted agglomeration of clusters inside the domains,[39] the samples were rapidly cooled in a liquid nitrogen bath from room temperature. After cooling to 5 K, a small magnetic field of 5 mT was applied, and the ZFC magnetization curve was recorded while the temperature was gradually increased to 225 K. To record the FC magnetization curve, the sample was then cooled back down to 5 K at the same magnetic field. The saturation magnetization value (M_{sat}) was normalized to the weight of iron by the mass fraction of Fe in magnetite and maghemite (typically 0.71 for magnetite and 0.69 for maghemite). The weight of iron was determined using inductively coupled plasma optical emission spectroscopy (ICP-OES).

2.2.3. Fe content determination. The Fe weight in the iron oxide nanoparticles dispersion in water was determined by inductively coupled plasma optical emission spectroscopy (ICP-OES) using an iCAP 7600 device. The sample was prepared by digesting the original sample used in SQUID measurements, followed by diluting a series of each digestion solution to obtain precise concentrations, which are crucial for accurate and reliable analytical results.

2.2.4. SAXS. Small-angle X-ray scattering (SAXS) measurements were performed at the KWS-X beamline at JCNS-MLZ, Garching, Germany. An incident X-ray wavelength of Ga Kα with λ = 1.3414 Å. SAXS measurements were carried out using two sample detector distances of 0.5 m and 1.7 m, resulting in a wide range of the scattering wave vector of 0.003 $Å^{-1} < Q <$ 1 $Å^{-1}$. Nanoparticle dispersions in water were sealed in quartz capillaries with 2 mm diameter and 0.01 mm wall thickness. The SAXS data were calibrated to absolute units and corrected for the background scattering contributions of the empty capillary.

2.2.5. Magnetic SANS. Unpolarized small-angle neutron scattering (SANS) was measured at the QUOKKA instrument at ANSTO, NSW, Australia, using a neutron wavelength of 5 Å and a wavelength resolution of 10%.[40,41] For the SANS experiment, the C71 particles dispersed in D_2O were placed in a 1 mm quartz cuvette (Hellma) positioned within a sample holder designed for an electromagnet. The latter was used to apply vertical magnetic fields from 0 up to 1.1 T perpendicular to the neutron beam direction. Table 1 represents the neutron scattering length density (ρ) and magnetic scattering length density (ρ_{mag}) for the investigated components and solvents. The measurements were done at room temperature and at three detector distances (2, 12, and 20 m) to obtain a Q-range of (0.004–0.7 $Å^{-1}$). The data reduction was performed using the IGOR Pro software.[42]

The SANS scattering intensity of the magnetic particle is a combination of the nuclear, $I_N(Q)$, and the magnetic, $I_M(Q)$, scattering intensity. The scattering intensity is proportional to the scattering contrast, the difference between the scattering length densities of the solvent and the particle. The dispersion of particles in D_2O leads to a low nuclear contrast $\Delta\rho$ (see Table 1). This leads to a reduction in the intensity of nuclear scattering from the cluster particles, allowing the magnetic scattering contribution to be highlighted.[43] The scattering intensity in a zero magnetic field is then written as[44]

$$I(Q)_{H=0} = I_N(Q)|_{\Delta\rho\approx 0} + \frac{2}{3} I_M(Q) \quad (1)$$

For a magnetic field applied perpendicular to the direction of the neutron beam, the magnetic moments of clusters are aligned by the field, which results in the magnetic scattering contribution being anisotropic in the detector plane. The scattering intensity is then expressed as[45]

$$I(Q,\theta)_{H\neq 0} = I_N(Q)|_{\Delta\rho\approx 0} + I_M(Q)\sin^2\theta \quad (2)$$

$$I_M(Q) = \frac{8\pi^3}{V} b_H{}^2 \left|\tilde{M}_z\right|^2 \quad (3)$$

Table 1 ρ and ρ_{mag} in the unit of 10^{-6} $Å^{-2}$ for the investigated components and solvents

Component	Fe_xO_y	Citrate	H_2O	D_2O
Density g cm^{-3}	5.74	1.70	1.00	1.10
ρ	6.91	1.50	−0.56	6.34
ρ_{mag}	0.94	—	—	—

The magnetic scattering length density (ρ_{mag}) of a single iron oxide core is taken from ref. 10. It is assumed that the value of ρ_{mag} for the cluster particles is comparable to that of the single cores.

The quantities V, b_H, $\tilde{M}_z$ and θ refer to the scattering volume, a constant parameter, the Fourier transform of the z-components of the magnetization vector field, the azimuthal angle between the applied magnetic field H and the scattering vector Q, respectively. The purely nuclear scattering contribution was obtained from the 2D scattering pattern in the sector of $\pm 10^\circ$ for $Q \| H$ ($\sin^2\theta \approx 0$). The field-dependent magnetic scattering amplitude is accessible from the 2D scattering pattern in a sector of $\pm 10^\circ$ for $Q \perp H$ ($\sin^2\theta \approx 1$). The contrast variation experiment in a zero magnetic field was also performed by dispersing the C71 particles in mixtures of H_2O and D_2O to vary the scattering length density of the solvent. This allowed for obtaining additional information about the structural organization of the cluster particles.

2.2.6. Mössbauer spectroscopy. Mössbauer absorption spectra were obtained in standard transmission geometry using a source of ^{57}Co(Rh) and a driving unit in constant acceleration mode. A LHe cryostat (Oxford SM4000-10) with split-pair geometry of superconducting magnet coils was utilized to carry out experiments at 5 K in an external magnetic field of 8 T parallel to the γ-ray incidence direction. For the particle oxidation study, sample fluids with particles dispersed in water at initial concentrations of 23 mg ml^{-1} iron for the C71 sample, 21 mg ml^{-1} iron for the B47 sample, and 8.8 mg ml^{-1} iron for the D40 sample, were initially stored in sealed containers under N_2 gas after preparation until the recording of the first Mössbauer spectrum, while during the study the oxidation behaviour was analyzed with the fluids being stored under ambient conditions. Experimental spectra were evaluated via a least-squares fitting routine using the "Pi" program package.[46]

3. Results and discussion

3.1. Morphology and structure

Fig. 1(a)–(c) shows transmission electron microscopy images of samples C71, B47 and D40. Samples C71 (Fig. 1) and B47 (Fig. 1b) display raspberry-like structures consisting of polydisperse small nanoparticle cores in larger clusters, which form network-like structures. The C71 system exhibits less extended structures. On the other hand, the D40 sample (Fig. 1c) shows a different morphology with the presence of smaller particles (1–2 nm). In this case, the dextran coating serves as a polymer matrix that embeds the NPs and forms randomly shaped aggregates. Table 2 summarizes the r_0 and σ parameters of the log-normal distribution of the single core nanoparticles. These parameters were determined from the fit according to the following expression:

$$f(x) = \frac{1}{\sqrt{2\pi}\sigma x} \cdot \exp\left(-\frac{(\ln(x/r_0))^2}{2\sigma^2}\right) \quad (4)$$

To further investigate the size and structure of the clusters, SAXS intensity curves (see Fig. 2a) were recorded for samples C71, B47 and D40. In SAXS, any effect of the coating molecules on the scattering will be negligible due to the much higher electron density of iron oxide. The presence of a Guinier-like region at low Q in the scattering curve of samples C71 and D40 indicates that the dimension of the scattering particles is less than $1/Q_{min}$ *i.e.* the inverse of the minimum Q. On the contrary, the scattering curve of sample B47 at $Q < 0.03$ Å^{-1} follows a power-law intensity of $I \simeq Q^{-2.2}$. The power law behaviour is consistent with the presence of larger scattering objects arising from cluster aggregation generating fractal like-structures.[47,48]

The pair distance distribution function, $P(r)$, was obtained by applying the indirect Fourier transform (IFT) to the scattering intensity using the GNOM software.[49] Fig. 2b displays the $P(r)$ profile for both the C71 and D40 samples. The B47 sample had stronger aggregation, so it was not possible to calculate the corresponding IFT. The profiles show a difference in overall particle size, as indicated by zero values occurring at different positions of $r = D_{max}$. The $P(r)$ of the C71 exhibits a shape that is more reminiscent of spherical particles, while the $P(r)$ of the D40 sample is characteristic of elongated particles.

In summary, the SAXS and TEM results show variations in the cluster sizes and the single core nanoparticles, which can be attributed to the coating materials used and the synthesis route. The SAXS result of the polymer dextran shows smaller clusters compared to the citrate and APTES molecules. However, the SAXS result of the APTES coating shows fractal aggregate clusters, which makes it less stable than C71. This information is valuable for improving the design and synthesis of nanoparticles for medical use.

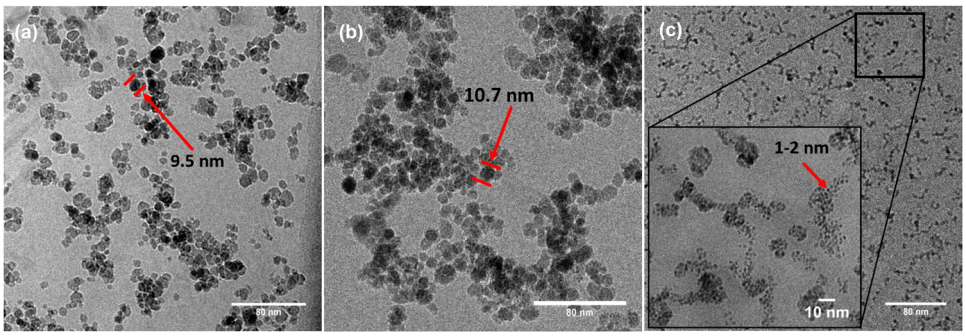

Fig. 1 Cryo-TEM images for the (a) C71, (b) B47, (c) and D40 samples, in cryogenic environment.

Table 2 r_0 and σ of the log-normal distribution of single cores determined by TEM, and cluster size D_{max} as obtained from SAXS

		TEM		SAXS
Coating material	Code	r_0 (nm)	σ	D_{max} (nm)
Citrate molecule	C71	9.5(1)	0.30(6)	56
APTES	B47	10.7(4)	0.30(5)	>120
Dextran	D40	2.0(8)	0.20(1)	36

3.2 Aging study

To study nanoparticle aging behaviour as a function of time, Mössbauer spectroscopy and magnetometry measurements were performed on particle dispersions in water repeatedly over a timespan of several weeks. Exemplary Mössbauer spectra of sample C71 recorded at 5 K in a magnetic field of 8 T are shown in Fig. 3, comparing the particle state after a certain time since the synthesis (up to 37 days), assuming a maximum time the particles were under ambient atmosphere between the synthesis and the start of the measurement of ca. 0.1 d. The spectra were reproduced via three sextet subspectra, based on their hyperfine parameters being assigned to Fe^{3+} in tetrahedral coordination (A sites, green), Fe^{3+} in octahedral coordination (B sites, blue) and Fe^{2+} in octahedral coordination (B site, violet). The ferrimagnetic structure of the particles is apparent from the resolution of the A- and B-site sublattice contributions after the application of the magnetic field. Based on the low intensity of absorption lines 2 and 5,[50] the particles display a moderate average spin canting angle of ca. 14°. The spin canting angle is defined as the angle between the spin and incidence directions of the γ-ray, with the latter here being identical to the magnetic field direction. Upon aging, the intensity of the B-site Fe^{2+} subspectrum decreases while the corresponding Fe^{3+} component increases, leading to more symmetrical B-site absorption lines over aging time. This is due to the shoulder formed by the B-site Fe^{2+} subspectrum becoming less pronounced, making the oxidation from magnetite to maghemite visible to the naked eye. The magnetite fraction is determined for each spectrum by comparing the

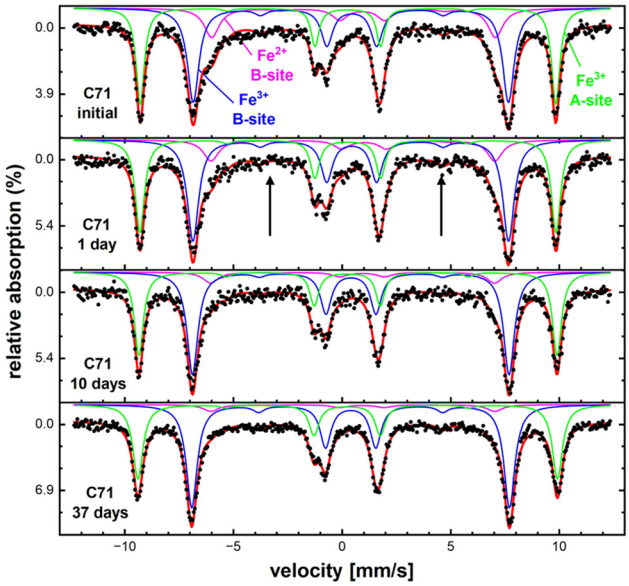

Fig. 3 Mössbauer spectra for sample C71 after various aging times of exposure to air, recorded at 5 K and an applied magnetic field of 8 T. In the C71 1 day spectrum, the vertical arrows mark Mössbauer lines 2 and 5, whose relative intensity indicates the degree of spin canting.[51]

Fe^{2+} fraction in pure magnetite (33.3%) and maghemite (0%). The magnetite fractions in samples C71, B47 and D40 are displayed in Table 3.

A complementary approach was used to determine the net magnetic properties and quantify the oxidation rate. This involved analyzing the time dependent change in saturation magnetization M_{sat}. The determination of M_{sat} at room temperature is presented in Table 4. To obtain this value, M_{sat} was extrapolated from high-field magnetization data using the law of approach to saturation as described by $M(H) = M_{sat}(1 - a/H - b/H^2)$. The magnetite fraction then is estimated by normalizing the net magnetization to the total Fe mass and comparing it to M_{sat} for bulk magnetite, 121 A m^2 kg_{Fe}^{-1}, and maghemite, 108 A m^2 kg_{Fe}^{-1}.[52] The obtained magnetite and maghemite

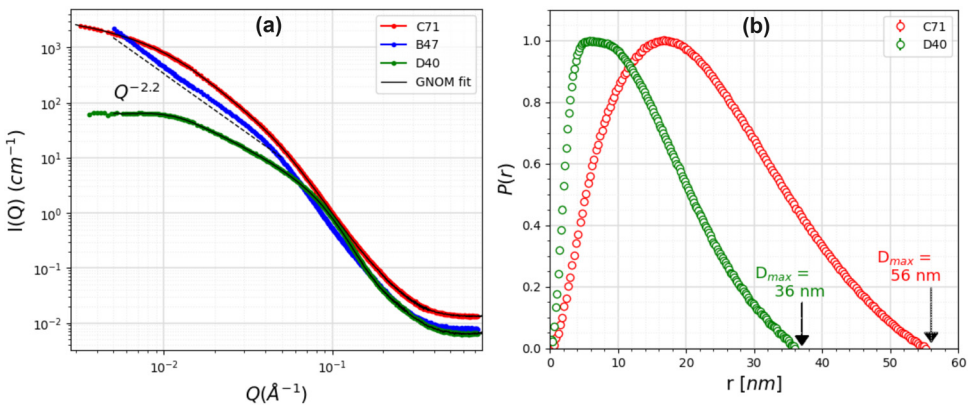

Fig. 2 (a) SAXS curves for the diluted samples with a concentration of 5.5 mg ml^{-1} iron for the C71 and B47 samples and up to 3.3 mg ml^{-1} iron for the D40 sample, and (b) pair-distance distribution functions $P(r)$ for samples C71 and D40, indicating that large particles are formed by the single-core nanoparticles.

Table 3 Magnetite fraction as a function of oxidation time obtained from Mössbauer spectroscopy analysis. The initial state is presented after 0.1 days of exposure to air during synthesis and preparation for the experiments

C71		B47		D40	
Aging time (day) (in air)	Magnetite fraction (%)	Aging time (day) (in air)	Magnetite fraction (%)	Aging time (day) (in air)	Magnetite fraction (%)
0.1	59.7 ± 6	0.1	62.7 ± 9.3	0.1	2.7 ± 3.3
1.1	41.1 ± 6.9	1.1	—	1.1	—
10.1	24.1 ± 7.2	9.1	24.3 ± 5.4	9.1	4.5 ± 7.8
37.1	15.3 ± 5.4	33.1	17.1 ± 7.5	35.1	0 ± 2.1
114.1	—	114.1	0.9 ± 1.2	114.1	—
252 (in N_2)	16 ± 4.4	242 (in N_2)	27.7 ± 4.5	249 (in N_2)	0 ± 1.9

Table 4 Magnetite fraction and saturation magnetization as a function of oxidation time obtained from magnetometry

Aging time (day) (in air)	C71		B47		D40	
	Magnetite fraction (%)	M_s (A m^2 kg^{-1})	Magnetite fraction (%)	M_s (A m^2 kg^{-1})	Magnetite fraction (%)	M_s (A m^2 kg^{-1})
0.1	64 ± 8	81.4 ± 0.8	54 ± 9	80.6 ± 1.6	0	69.9 ± 1
1.1	44 ± 9	79.2 ± 0.9	33 ± 1.8	78.3 ± 1.3	0	69.7 ± 0.6
10.1	—	—	28 ± 1.8	77.8 ± 1.3	0	69.9 ± 0.3
33.1	17 ± 10	76.3 ± 1.1	10 ± 6	75.7 ± 0.6	0	69.9 ± 1
180	3.8 ± 5.3	75 ± 0.5	0	73.5 ± 0.6	0	69.9 ± 1

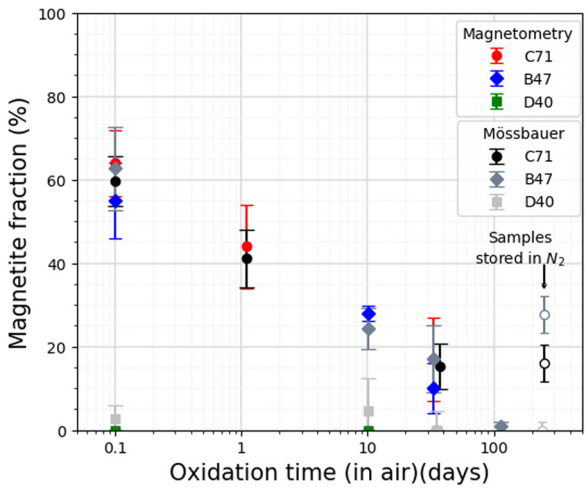

Fig. 4 Comparison of the magnetite fraction obtained over various oxidation times in air from Mössbauer spectroscopy and magnetometry. The samples stored under N_2 (empty symbols) are included for comparing the magnetite fraction to the samples stored in the air.

fractions are used for normalizing saturation magnetization. As shown in Fig. 4, magnetite fractions obtained from Mössbauer spectroscopy and magnetometry are in good agreement. For samples C71 and B47, the initial measurements already indicate ca. 40% of the particle mass was oxidized after a limited exposure time of less than ca. 2 h, which corresponds to a maghemite shell thickness of *ca.* 0.8–1 nm in single core nanoparticles. This would match the expectation of fast formation of a maghemite surface layer, followed by decelerated further oxidation, resulting in a remaining magnetite fraction of ca. 10–20% in both samples after one month of storage under ambient conditions. After 114 days for sample B47 only minimum Fe^{2+} is detected in Mössbauer spectroscopy, indicating complete conversion to maghemite within the error margin. In contrast, sample D40 oxidizes faster than the other samples, showing no considerable Fe^{2+} component already in the initial spectrum, which is also indicated by magnetometry data. For comparison, a second batch of samples C71 and B47 was also stored for six months after preparation under N_2. This batch exhibited higher stability against oxidation by preserving a magnetite fraction of around 20–30%, which is comparable to the fraction observed after 10–30 days of exposure to air.

The saturation magnetization determined for samples C71 and B47 is comparable to the bulk value. However, for sample D40, the saturation magnetization value is 6.6 ± 0.9% lower than for maghemite. This decrease in magnetization may have several causes, including minor fitting artifacts in the extrapolation of M_s due to the non-saturating tendency of the $M(H)$ loops, or crystal defects such as the presence of antiphase boundaries, modified atomic coordination, and an increased number of Fe vacancies.[10,53–55] The relatively large error in the saturation magnetization is due to an inaccurate determination of Fe-content using ICP-OES. Treating the entire sample along with the holder might result in significant errors when determining the Fe content.

3.3. Magnetic properties

The hysteresis loops at room temperature (Fig. 5a) for all samples indicate a negligible coercive field, confirming that the nanoparticle clusters exhibit superparamagnetic behaviour. A detailed assessment of the magnetic properties of the clusters was conducted using ZFC/FC curves (Fig. 5b). The blocking temperature, T_B, is the temperature at which the transition occurs from the unblocked superparamagnetic to the blocked state. This transition is affected by several factors, such as particle size distribution and magnetic interparticle interactions.[56–58]

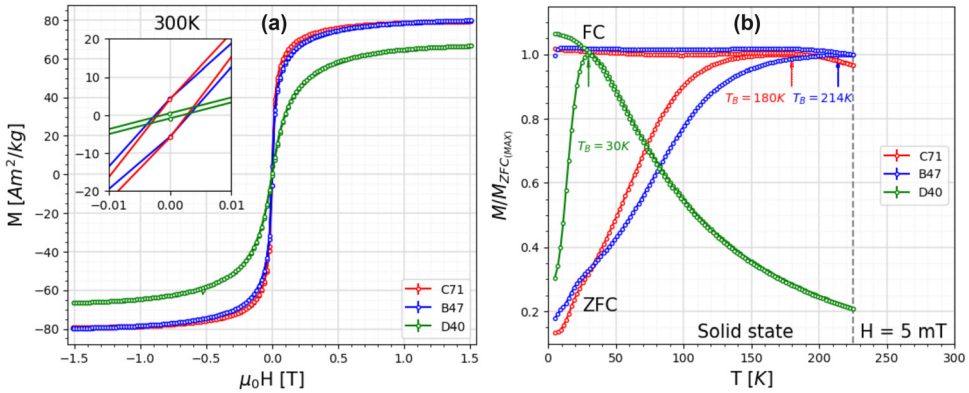

Fig. 5 (a) Hysteresis curves at room temperature in the range of ±1.5 T. (b) Normalized ZFC/FC curves performed in the temperature range of 5–225 K and a magnetic field of 5 mT. The upper limit temperature is set at 225 K to avoid traversing the melting temperature of water.

Here, samples C71 and B47 exhibit similar single-core particle sizes but differ in the organization formed by these particles. The two samples have different T_B values, with C71 having a T_B of 180 K and B47 having a T_B of 214 K. The determination of T_B is based on the highest value found in the ZFC curve. The broadening of peaks in the ZFC curves can be attributed to either a variation in the particle volume or strong magnetic interactions.[59] The SAXS results confirm that magnetic interaction is the main reason for the broadening featured in strongly aggregated single-core nanoparticles. Also, the flattened shape of the FC curve provides evidence for the existence of magnetic inter-particle interactions. Sample D40 displays a T_B of about 30 K, which corresponds to the small particle sizes confirmed in TEM measurements.

A qualitative assessment of the particle size distribution can be found from the difference in temperatures between the peak position of the ZFC curve and the splitting temperature between ZFC and FC curves.[60,61] Sample C71 with a T_B of 180 K would correspond to a particle size of 10–15 nm, with a surprisingly narrow size distribution considering the shape of the ZFC/FC curves and the qualitative difference in temperature. However, such an interpretation would be in direct contradiction to the TEM analysis, which reveals a large polydispersity of the single nanoparticle cores. In addition, the blocking temperature from the ZFC curve would correspond to much smaller sizes of particles than obtained in SAXS. Therefore, further studies with small-angle neutron scattering are necessary to obtain the coherent magnetic size of the clusters and clarify the ZFC/FC results.

3.4. Magnetic size determination

3.4.1. SANS at zero field. Fig. 6a displays the SANS of C71 dispersed in water with various D_2O content: from 0 to 100%. Contrast variation SANS measurements enable us to characterize the colloidal solution precisely, particularly in determining the neutron scattering length density (SLD) of cluster particles.[62] The nuclear scattering decreases gradually as the D_2O content increases, reaching its minimum at 100% D_2O. The scattering curves maintain their shape regardless of the nuclear contrast, indicating that the cluster particles can be considered homogeneous and that the scattering length density is largely independent of experimental Q. Fig. 6a (inset) shows the quadratic dependence of the scattering intensity as a function of the solvent contrast at the minimum experimental Q value, which yields the contrast match point of the large

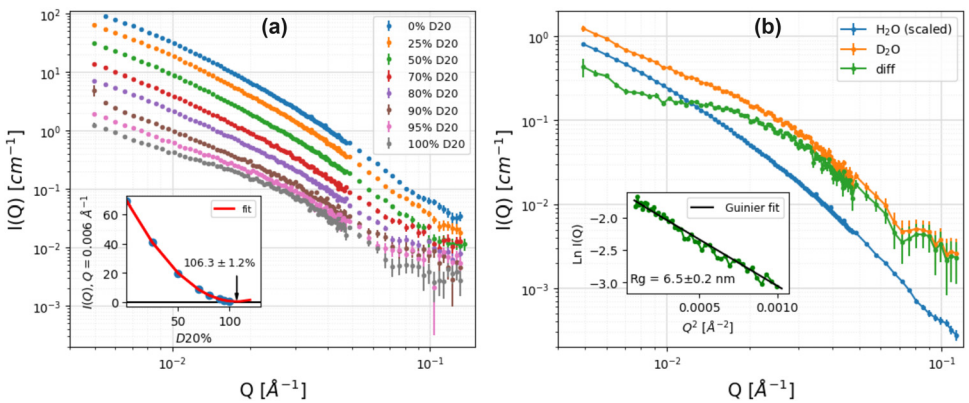

Fig. 6 (a) SANS intensity curves of C71 for various H_2O/D_2O mixtures. The inset shows the scattering intensity as a function of D_2O content at a Q value of 0.06 Å^{-1}. It is fitted with a parabolic curve to obtain the nuclear contrast match point. (b) Pure magnetic scattering in D_2O sample (at zero magnetic field) as extracted by scaling the H_2O data down by a factor of 131 and subtracting from the 100% D_2O curve. The Guinier fit of the difference curve is shown in the inset.

cluster at 106.3 ± 1.2% of D_2O. Therefore, the contribution of the citrate shell is negligible.

The scattering curves of the sample with high D_2O content between 0% and 80% indicate the presence of large structures, which prevents a simple Guinier analysis. In comparison to SAXS data (see Fig. 2a), the SANS curves point to an advanced aggregation in the sample, which occurred during the period between the preparation of contrast variation samples and the measurement (approximately 6 months). We believe that this developed aggregation does not influence the characterization of initial clusters of nanoparticles in the studied Q-range. A clearly observable feature in the curves for large D_2O content (above 95%) is present in the mid-Q-range $0.02 < Q < 0.06$ Å^{-1} (Fig. 6a). Although it was not possible to fully compensate for the nuclear signal, this feature is primarily a result of the magnetic scattering associated with single particles (or magnetic correlations between them) constituting the large clusters. It is important to note that the magnetic scattering contribution is independent of the nuclear contrast between the particle and solvent. Using pure H_2O as a solvent results in a significant scattering length density contrast between the iron oxide nanoparticles and the water. Thus, the scattering intensity in this case results mainly from the nuclear signal, while the magnetic contribution is negligible.[63] To separate the magnetic scattering from the residual nuclear scattering in D_2O, the H_2O curve is divided by a factor of 131 and subtracted from the 100% D_2O curve. The scaling factor is determined manually and approximately corresponds to the ratio of particle contrasts, $\Delta\rho^2$, in H_2O and D_2O solvents. Its exact determination is difficult due to uncertainties in the determination of the average SLD of the particles, as we could not observe the zero-angle scattering intensity $I(0)$. A Guinier region in the difference curve appears as shown in Fig. 6b and can be attributed to magnetic spherical objects with a $D = 2\sqrt{5/3}R_g \approx 16.8 \pm 0.4$ nm (Fig. 6b (inset)). This size is in agreement with the obtained T_B from the ZFC data, which corresponds to a contribution of single nanoparticles (or their magnetic correlations) in the clusters.

3.4.2. SANS with applying magnetic field. Fig. 7 shows the two-dimensional neutron scattering patterns obtained for C71 dispersed in D_2O without and with the application of an external magnetic field of 1.1 T. The aim is to determine the variation in magnetic size with the field. Upon application of a magnetic field of 1.1 T, the 2D SANS patterns exhibit a predictable anisotropy. This anisotropy originates from an anisotropic magnetic scattering distribution.[62] In those under-field SANS measurements, it is necessary to separate I_M from I_N. Therefore, the 2D patterns are analyzed in sectors parallel to the magnetic field direction, with pure nuclear scattering, and perpendicular to the magnetic field direction, where a combination of nuclear and magnetic scattering is detected (Fig. 8a). In the range of magnetic fields from 0 to 0.11 T, the scattering intensity is comparable for both the parallel and perpendicular sectors. However, for magnetic fields greater than 0.11 T, the scattering intensity decreases in the parallel sector and increases in the perpendicular one due to the redistribution of magnetic scattering during progressive sample magnetization. Pure magnetic scattering is obtained by subtracting the perpendicular scattering intensity (composed of both nuclear and magnetic components) from the parallel scattering intensity (composed only of nuclear components) in saturating fields (see Fig. 8b). The appearance of a Guinier region indicates the presence of large magnetic clusters and negligible magnetic inter-cluster interaction. Therefore, there is no correlation between the collective magnetic moments of two different clusters. A Guinier fit to the magnetic scattering at 1.1 T yields a radius of gyration, $R_g \approx 13.5 \pm 0.3$ nm (magnetic sphere diameter 34.8 ± 0.8 nm). The observed results can be attributed to the significant magnetic inter-particle interaction within the clusters, resulting in a large net magnetic size, that is approximately half of the cluster size. The latter result is important in terms of obtaining nanoparticle assemblies with large magnetic susceptibility, where the coherent

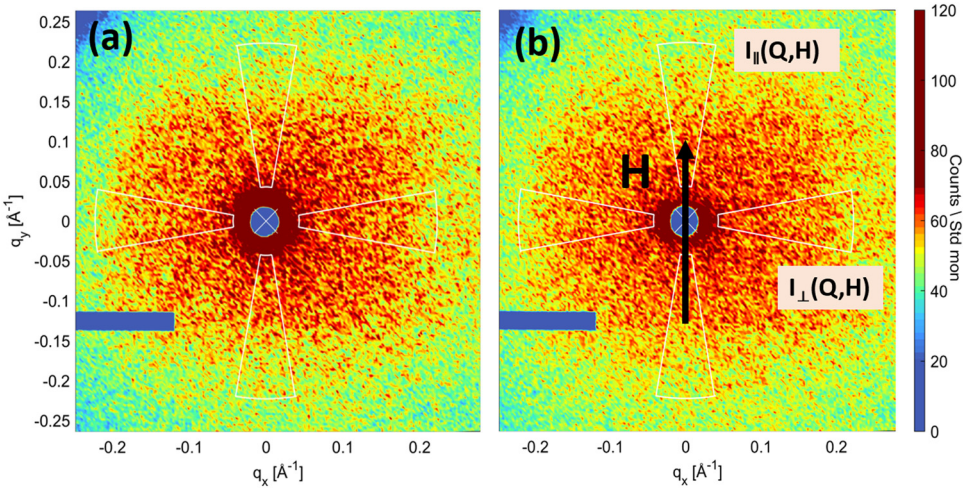

Fig. 7 Two-dimensional SANS patterns for sample C71 dispersed in D_2O. (a) Isotropic pattern with no applied magnetic field, (b) anisotropic pattern with the magnetic field of 1.1 T along the vertical direction, as shown by an arrow.

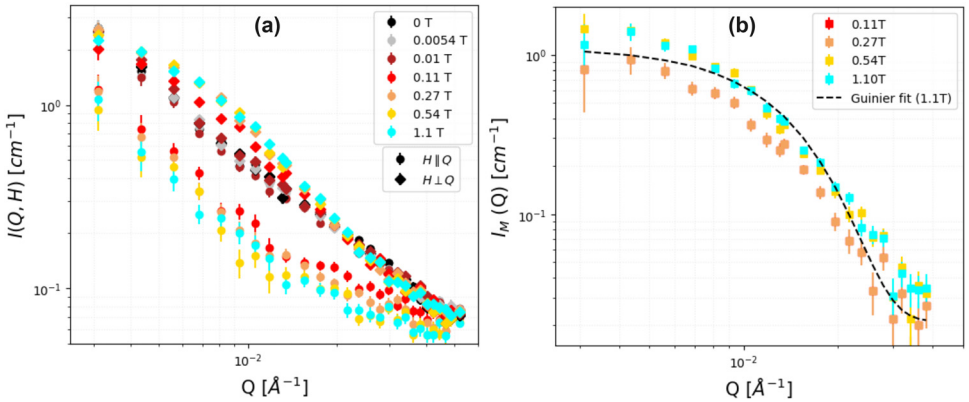

Fig. 8 (a) Scattering intensity of sample C71 dispersion in D_2O solvent in the parallel sector($H \parallel Q$) and perpendicular sector ($H \perp Q$), (b) pure magnetic scattering at high fields close to saturation.

rotation of the superspin within the cluster is desirable, *i.e.*, in which the superspins of the constituent particles rotate in unison.[64]

4. Conclusion

The study investigated the impact of three types of coating materials on the structure, magnetic properties, and long-term stability of biocompatible iron oxide nanoparticles. The coating types are citrate, (3-aminopropyl) triethoxysilane (APTES), and dextran. The study's findings indicate that the type of coating significantly influences the organization of nanoparticles into distinct structures. The SAXS results showed different cluster sizes associated with each type of coating: 36 nm for dextran, 56 nm for citrate, and fractal cluster aggregates for APTES. The underlying particle core sizes are hereby: 2 nm for dextran, 9.5 nm for citrate, and 9.8 nm for APTES. In addition, the oxidation rates of the iron oxide cores were also studied for all three types of coatings. All systems exhibited rapid oxidation after less than 0.1 days (the time between the end of the synthesis and the sealing of the samples under N_2 atmosphere). This led to the complete oxidation of the cores to maghemite for the dextran coating, while the citrate and APTES coating showed slower oxidation with 10–20% magnetite fraction after one month. After 3 months, the magnetite fraction is not detectable neither in Mössbauer spectroscopy nor in magnetometry. The varying oxidation behaviours can be attributed to differences in particle size resulting from the used coating agent and the synthesis route. Magnetic SANS at zero field on the citrate-coated nanoparticles revealed the magnetic size, which agrees with the ZFC data. The zero-field magnetic size is slightly larger than the size of a single nanoparticle obtained from TEM. At saturation field, the magnetic size of the clusters is increased, leading to approximately half the cluster size, corroborating the presence of magnetic domains inside the clusters. Overall, it is of great importance to be able to control the desired material properties through the choice of coating and the route of synthesis. In addition, the detailed knowledge of the aging processes of the particles is of equally large importance for officially approved quality standards. Such knowledge can guide the development of more stable nanoparticles that retain their magnetic properties for extended periods of time. Magnetic susceptibility, which, among other properties, depends mainly on the cluster size and core spacing, has a direct impact *e.g.* on the T_2 relaxation time in Magnetic Resonance Imaging (MRI) and on the specific absorption rate (SAR) for hyperthermia applications. It was, for instance, found that in chains of particles, the SAR might increase compared to single particles.[65] Consequently, a detailed knowledge of the particle arrangement and its impact on the magnetic properties can help in tuning the synthesis route to obtain the desired characteristics of the nanoparticle systems.

Author contributions

Amal Nasser: planning the research study, sample preparation, performing SAXS and SANS experiments, data collection and analysis, writing the manuscript. Asmaa Qdemat & Baohu Wu: performing SAXS experiment and reducting the data. Harald Unterweger & Rainer Tietze: synthesis of samples, discussing the project motivations and the obtained results. Xiao Sun: helping in designing the SAXS experiments and data reduction. Joachim Landers: Mössbauer data analysis, performing mössbauer spectroscopy experiments with Juri Kopp. Marie-Sousai Appavou: performing cryo-TEM experiment. Elliot Paul Gilbert: performing SANS experiment and helping in data reduction assisted with Anastasiia Murmiliuk & Asmaa Qdemat. Artem Feoktystov & Oleg Petracic: supervision, project administration, planning the research work, assisting in data reduction and analysis, discussion, helping in manuscript preparation. All authors read, edited, and approved the final manuscript.

Data availability

The data supporting this article have been included as part of the ESI.†

Conflicts of interest

There are no conflicts to declare.

Acknowledgements

This work is funded by the German Federal Ministry of Education and Research in the framework of the Palestinian-German Science Bridge (PGSB) and by DFG grant LA 5175/1-1. The authors acknowledge the support of the Australian Centre for Neutron Scattering, ANSTO, and the Australian Government through the National Collaborative Research Infrastructure Strategy, supporting the QUOKKA neutron research infrastructure used in this work *via* ACNS proposal P14278.

References

1 H. Ittrich, K. Peldschus, N. Raabe, M. Kaul and G. Adam, Superparamagnetic iron oxide nanoparticles in biomedicine: applications and developments in diagnostics and therapy, *Fortschr. Röntgenstr.*, 2013, **185**(12), 1149–1166.
2 S. M. Dadfar, K. Roemhild, N. I. Drude, S. von Stillfried, R. Knüchel and F. Kiessling, *et al.*, Iron oxide nanoparticles: Diagnostic, therapeutic and theranostic applications, *Adv. Drug Delivery Rev.*, 2019, **138**, 302–325.
3 P. B. Santhosh and N. P. Ulrih, Multifunctional superparamagnetic iron oxide nanoparticles: promising tools in cancer theranostics, *Cancer Lett.*, 2013, **336**(1), 8–17.
4 S. Mornet, S. Vasseur, F. Grasset and E. Duguet, Magnetic nanoparticle design for medical diagnosis and therapy, *J. Mater. Chem.*, 2004, **14**(14), 2161–2175.
5 A. Lindemann, K. Lüdtke-Buzug, B. M. Fräderich, K. Gräfe, R. Pries and B. Wollenberg, Biological impact of superparamagnetic iron oxide nanoparticles for magnetic particle imaging of head and neck cancer cells, *Int. J. Nanomed.*, 2014, 5025–5040.
6 R. Tietze, J. Zaloga, H. Unterweger, S. Lyer, R. P. Friedrich and C. Janko, *et al.*, Magnetic nanoparticle-based drug delivery for cancer therapy, *Biochem. Biophys. Res. Commun.*, 2015, **468**(3), 463–470.
7 S. Laurent, S. Dutz, U. O. Häfeli and M. Mahmoudi, Magnetic fluid hyperthermia: focus on superparamagnetic iron oxide nanoparticles, *Adv. Colloid Interface Sci.*, 2011, **166**(1–2), 8–23.
8 V. Patsula, M. Moskvin, S. Dutz and D. Horák, Size-dependent magnetic properties of iron oxide nanoparticles, *J. Phys. Chem. Solids*, 2016, **88**, 24–30.
9 A. G. Roca, L. Gutiérrez, H. Gavilán, M. E. F. Brollo, S. Veintemillas-Verdaguer and M. del Puerto Morales, Design strategies for shape-controlled magnetic iron oxide nanoparticles, *Adv. Drug Delivery Rev.*, 2019, **138**, 68–104.
10 T. Köhler, A. Feoktystov, O. Petracic, E. Kentzinger, T. Bhatnagar-Schöffmann and M. Feygenson, *et al.*, Mechanism of magnetization reduction in iron oxide nanoparticles, *Nanoscale*, 2021, **13**(14), 6965–6976.
11 M. Benitez, D. Mishra, P. Szary, G. B. Confalonieri, M. Feyen and A. Lu, *et al.*, Structural and magnetic characterization of self-assembled iron oxide nanoparticle arrays, *J. Phys.: Condens. Matter*, 2011, **23**(12), 126003.
12 O. Petracic, X. Chen, S. Bedanta, W. Kleemann, S. Sahoo and S. Cardoso, *et al.*, Collective states of interacting ferromagnetic nanoparticles, *J. Magn. Magn. Mater.*, 2006, **300**(1), 192–197.
13 C. Vasilescu, M. Latikka, K. D. Knudsen, V. M. Garamus, V. Socoliuc and R. Turcu, *et al.*, High concentration aqueous magnetic fluids: structure, colloidal stability, magnetic and flow properties, *Soft Matter*, 2018, **14**(32), 6648–6666.
14 M. Mühlberger, C. Janko, H. Unterweger, R. P. Friedrich, B. Friedrich and J. Band, *et al.*, Functionalization of T lymphocytes with citrate-coated superparamagnetic iron oxide nanoparticles for magnetically controlled immune therapy, *Int. J. Nanomed.*, 2019, 8421–8432.
15 M. Escoda-Torroella, C. Moya, A. F. Rodrguez, X. Batlle and A. Labarta, Selective control over the morphology and the oxidation state of iron oxide nanoparticles, *Langmuir*, 2020, **37**(1), 35–45.
16 T. Krasia-Christoforou, V. Socoliuc, K. D. Knudsen, E. Tombácz, R. Turcu and L. Vékás, From single-core nanoparticles in ferrofluids to multi-core magnetic nanocomposites: Assembly strategies, structure, and magnetic behavior, *Nanomaterials*, 2020, **10**(11), 2178.
17 L. Gutiérrez, R. Costo, C. Grüttner, F. Westphal, N. Gehrke and D. Heinke, *et al.*, Synthesis methods to prepare single- and multi-core iron oxide nanoparticles for biomedical applications, *Dalton Trans.*, 2015, **44**(7), 2943–2952.
18 A. Gallo-Cordova, J. G. Ovejero, A. M. Pablo-Sainz-Ezquerra, J. Cuya, B. Jeyadevan and S. Veintemillas-Verdaguer, *et al.*, Unravelling an amine-regulated crystallization crossover to prove single/multicore effects on the biomedical and environmental catalytic activity of magnetic iron oxide colloids, *J. Colloid Interface Sci.*, 2022, **608**, 1585–1597.
19 L. Gutiérrez, L. De la Cueva, M. Moros, E. Mazaro, S. De Bernardo and J. M. De la Fuente, *et al.*, Aggregation effects on the magnetic properties of iron oxide colloids, *Nanotechnology*, 2019, **30**(11), 112001.
20 H. Shokrollahi, A review of the magnetic properties, synthesis methods and applications of maghemite, *J. Magn. Magn. Mater.*, 2017, **426**, 74–81.
21 D. Maity and D. Agrawal, Synthesis of iron oxide nanoparticles under oxidizing environment and their stabilization in aqueous and non-aqueous media, *J. Magn. Magn. Mater.*, 2007, **308**(1), 46–55.
22 R. Grau-Crespo, A. Y. Al-Baitai, I. Saadoune and N. H. De Leeuw, Vacancy ordering and electronic structure of γ -Fe2O3 (maghemite): a theoretical investigation, *J. Phys.: Condens. Matter*, 2010, **22**(25), 255401.
23 B. D. Cullity and C. D. Graham, *Introduction to Magnetic Materials*, John Wiley & Sons, 2011, pp. 115–150.
24 G. C. Lavorato, A. A. de Almeida, C. Vericat and M. H. Fonticelli, Redox phase transformations in magnetite nanoparticles: impact on their composition, structure and biomedical applications, *Nanotechnology*, 2023, **34**(19), 192001.

25 K. Jiang, Q. Zhang, D. T. Hinojosa, L. Zhang, Z. Xiao and Y. Yin, *et al.*, Controlled oxidation and surface modification increase heating capacity of magnetic iron oxide nanoparticles, *Appl. Phys. Rev.*, 2021, **8**, 031407.
26 C. Dennis, A. Jackson, J. Borchers, P. Hoopes, R. Strawbridge and A. Foreman, *et al.*, Nearly complete regression of tumors via collective behavior of magnetic nanoparticles in hyperthermia, *Nanotechnology*, 2009, **20**(39), 395103.
27 L. Li, K. Y. Mak, C. W. Leung, K. Y. Chan, W. K. Chan and W. Zhong, *et al.*, Effect of synthesis conditions on the properties of citric-acid coated iron oxide nanoparticles, *Microelectron. Eng.*, 2013, **110**, 329–334.
28 H. Unterweger, R. Tietze, C. Janko, J. Zaloga, S. Lyer and S. Dürr, *et al.*, Development and characterization of magnetic iron oxide nanoparticles with a cisplatin-bearing polymer coating for targeted drug delivery, *Int. J. Nanomed.*, 2014, 3659–3676.
29 B. Friedrich, S. Lyer, C. Janko, H. Unterweger, R. Brox and S. Cunningham, *et al.*, Scavenging of bacteria or bacterial products by magnetic particles functionalized with a broad-spectrum pathogen recognition receptor motif offers diagnostic and therapeutic applications, *Acta Biomater.*, 2022, **141**, 418–428.
30 H. Unterweger, L. Dézsi, J. Matuszak, C. Janko, M. Poettler and J. Jordan, *et al.*, Dextran-coated superparamagnetic iron oxide nanoparticles for magnetic resonance imaging: Evaluation of size-dependent imaging properties, storage stability and safety, *Int. J. Nanomed.*, 2018, **13**, 1899.
31 W. Mekseriwattana, P. Guardia, B. T. Herrero, J. M. de la Fuente, C. Kuhakarn and A. Roig, *et al.*, Riboflavin-citrate conjugate multicore SPIONs with enhanced magnetic responses and cellular uptake in breast cancer cells, *Nanoscale Adv.*, 2022, **4**(8), 1988–1998.
32 M. S. Khan, B. J. Gowda, N. Nasir, S. Wahab, M. R. Pichika and A. Sahebkar, *et al.*, Advancements in dextran-based nanocarriers for treatment and imaging of breast cancer, *Int. J. Pharm.*, 2023, 123276.
33 G. B. Confalonieri, V. Vega, A. Ebbing, D. Mishra, P. Szary and V. M. Prida, *et al.*, Template-assisted self-assembly of individual and clusters of magnetic nanoparticles, *Nanotechnology*, 2011, **22**(28), 285608.
34 L. Lartigue, P. Hugounenq, D. Alloyeau, S. P. Clarke, M. Lévy and J. C. Bacri, *et al.*, Cooperative organization in iron oxide multi-core nanoparticles potentiates their efficiency as heating mediators and MRI contrast agents, *ACS Nano*, 2012, **6**(12), 10935–10949.
35 S. Laurent, D. Forge, M. Port, A. Roch, C. Robic and L. Vander Elst, *et al.*, Magnetic iron oxide nanoparticles: synthesis, stabilization, vectorization, physicochemical characterizations, and biological applications, *Chem. Rev.*, 2008, **108**(6), 2064–2110.
36 R. Massart, Preparation of aqueous magnetic liquids in alkaline and acidic media, *IEEE Trans. Magn.*, 1981, **17**(2), 1247–1248.
37 N. Saxena, H. Agraval, K. C. Barick, D. Ray, V. K. Aswal and A. Singh, *et al.*, Thermal and microwave synthesized SPIONs: Energy effects on the efficiency of nano drug carriers, *Mater. Sci. Eng., C*, 2020, **111**, 110792.
38 H. C. Roth, S. P. Schwaminger, M. Schindler, F. E. Wagner and S. Berensmeier, Influencing factors in the CO-precipitation process of superparamagnetic iron oxide nano particles: A model based study, *J. Magn. Magn. Mater.*, 2015, **377**, 81–89.
39 S. Webers, M. Hess, J. Landers, A. M. Schmidt and H. Wende, Effect of phase transitions in polymer solutions on the magnetic response of embedded nanoparticles, *ACS Appl. Polym. Mater.*, 2020, **2**(7), 2676–2685.
40 E. P. Gilbert, J. C. Schulz and T. J. Noakes, 'Quokka'-the small-angle neutron scattering instrument at OPAL, *Phys. Rev. B: Condens. Matter Mater. Phys.*, 2006, **385**, 1180–1182.
41 K. Wood, J. P. Mata, C. J. Garvey, C. M. Wu, W. A. Hamilton and P. Abbeywick, *et al.*, QUOKKA, the pinhole small-angle neutron scattering instrument at the OPAL Research Reactor, Australia: design, performance, operation and scientific highlights, *J. Appl. Crystallogr.*, 2018, **51**(2), 294–314.
42 S. R. Kline, Reduction and analysis of SANS and USANS data using IGOR Pro, *J. Appl. Crystallogr.*, 2006, **39**(6), 895–900.
43 D. Eberbeck, C. L. Dennis, N. F. Huls, K. L. Krycka, C. Gruttner and F. Westphal, Multicore magnetic nanoparticles for magnetic particle imaging, *IEEE Trans. Magn.*, 2012, **49**(1), 269–274.
44 M. V. Avdeev, E. Dubois, G. Mériguet, E. Wandersman, V. M. Garamus and A. V. Feoktystov, *et al.*, Small-angle neutron scattering analysis of a water-based magnetic fluid with charge stabilization: contrast variation and scattering of polarized neutrons, *J. Appl. Crystallogr.*, 2009, **42**(6), 1009–1019.
45 S. Mühlbauer, D. Honecker, É. A. Périgo, F. Bergner, S. Disch and A. Heinemann, *et al.*, Magnetic small-angle neutron scattering, *Rev. Mod. Phys.*, 2019, **91**(1), 015004.
46 U. von Hörsten, 2023, **https://udue.de/pi**.
47 G. Beaucage, Small-angle scattering from polymeric mass fractals of arbitrary mass-fractal dimension, *J. Appl. Crystallogr.*, 1996, **29**(2), 134–146.
48 A. Y. Cherny, E. M. Anitas, V. A. Osipov and A. I. Kuklin, The structure of deterministic mass and surface fractals: Theory and methods of analyzing small-angle scattering data, *Phys. Chem. Chem. Phys.*, 2019, **21**(24), 12748–12762.
49 D. Svergun, Determination of the regularization parameter in indirect-transform methods using perceptual criteria, *J. Appl. Crystallogr.*, 1992, **25**(4), 495–503.
50 D. Peddis, N. Yaacoub, M. Ferretti, A. Martinelli, G. Piccaluga and A. Musinu, *et al.*, Cationic distribution and spin canting in $CoFe_2O_4$ nanoparticles, *J. Phys.: Condens. Matter*, 2011, **23**(42), 426004.
51 J. Landers, F. Stromberg, M. Darbandi, C. Schöppner, W. Keune and H. Wende, Correlation of superparamagnetic relaxation with magnetic dipole interaction in capped iron-oxide nanoparticles, *J. Phys.: Condens. Matter*, 2014, **27**(2), 026002.
52 X. Batlle, N. Pérez, P. Guardia, O. Iglesias, A. Labarta and F. Bartolomé, *et al.*, Magnetic nanoparticles with bulklike properties, *J. Appl. Phys.*, 2011, **109**(7), 07B524.

53 A. Lak, S. Disch and P. Bender, Embracing defects and disorder in magnetic nanoparticles, *Adv. Sci.*, 2021, **8**(7), 2002682.
54 M. Coduri, P. Masala, L. Del Bianco, F. Spizzo, D. Ceresoli and C. Castellano, *et al.*, Local structure and magnetism of Fe_2O_3 maghemite nanocrystals: The role of crystal dimension, *Nanomaterials*, 2020, **10**(5), 867.
55 M. P. Morales, S. Veintemillas-Verdaguer, M. Montero, C. Serna, A. Roig and L. Casas, *et al.*, Surface and internal spin canting in γ-Fe_2O_3 nanoparticles, *Chem. Mater.*, 1999, **11**(11), 3058–3064.
56 O. Petracic, Superparamagnetic nanoparticle ensembles, *Superlattices Microstruct.*, 2010, **47**(5), 569–578.
57 B. D. Plouffe, D. K. Nagesha, R. S. DiPietro, S. Sridhar, D. Heiman and S. K. Murthy, *et al.*, Thermomagnetic determination of Fe_3O_4 magnetic nanoparticle diameters for biomedical applications, *J. Magnetism Magnetic Mater.*, 2011, **323**(17), 2310–2317.
58 N. Nandakumaran, L. Barnsley, A. Feoktystov, S. A. Ivanov, D. L. Huber and L. S. Fruhner, *et al.*, Unravelling magnetic nanochain formation in dispersion for in vivo applications, *Adv. Mater.*, 2021, **33**(24), 2008683.
59 R. Frison, G. Cernuto, A. Cervellino, O. Zaharko, G. M. Colonna and A. Guagliardi, *et al.*, Magnetite– ite nanoparticles in the 5–15 nm range: correlating the core–shell composition and the surface structure to the magnetic properties. A total scattering study, *Chem. Mater.*, 2013, **25**(23), 4820–4827.
60 S. Bedanta, O. Petracic and W. Kleemann, *Handbook of magnetic materials*, Elsevier, 2015, vol. 23, pp. 1–83.
61 K. Mandel, F. Hutter, C. Gellermann and G. Sextl, Stabilisation effects of superparamagnetic nanoparticles on clustering in nanocomposite microparticles and on magnetic behaviour, *J. Magn. Magn. Mater.*, 2013, **331**, 269–275.
62 H. Stuhrmann, Neutron small-angle scattering of biological macromolecules in solution, *J. Appl. Crystallogr.*, 1974, **7**(2), 173–178.
63 M. V. Avdeev and V. L. Aksenov, Small-angle neutron scattering in structure research of magnetic fluids, *Phys.-Usp.*, 2010, **53**(10), 971.
64 C. Moya, M. Escoda-Torroella, J. Rodríguez-Álvarez, A. I. Figueroa, Í. García and I. B. Ferrer-Vidal, *et al.*, Unveiling the crystal and magnetic texture of iron oxide nanoflowers, *Nanoscale*, 2024, **16**(4), 1942–1951.
65 C. Martinez-Boubeta, K. Simeonidis, A. Makridis, M. Angelakeris, O. Iglesias and P. Guardia, *et al.*, Learning from nature to improve the heat generation of iron-oxide nanoparticles for magnetic hyperthermia applications, *Sci. Rep.*, 2013, **3**(1), 1652.